

The inclusion and role of micro mechanical residual stress on deformation of stainless steel type 316L at grain level

Edward William Horton ^{a,*}, Eralp Demir ^{a,b}, Dylan Agius ^{a,c}, Anna Kareer ^d, David M. Collins ^e, Mahmoud Mostafavi ^a, David Knowles ^a

^a Department of Mechanical Engineering, University of Bristol, Bristol, BS8 1TR, United Kingdom

^b Department of Engineering Science, University of Oxford, Parks road, Oxford OX1 3PJ, United Kingdom

^c Platforms Division, Defence Science and Technology Group, Melbourne 3207, Australia

^d Department of Materials, University of Oxford, Parks Road, Oxford OX1 3PH, United Kingdom

^e School of Metallurgy and Materials, University of Birmingham, Edgbaston, Birmingham B15 2TT, United Kingdom

ARTICLE INFO

Keywords:

Crystal plasticity
Finite element method
Residual stress
HR-EBSD

ABSTRACT

Validating crystal plasticity models requires careful consideration of all aspects. The initial conditions are important when comparing a model and experiment, as the initial residual stresses within the material can be significant but are often overlooked due to experimental limitations. Therefore, their inclusion has the potential to improve model predictions. This work explores the efficacy of using type-III residual elastic stresses, measured using high resolution electron backscatter diffraction (HR-EBSD), as pre-test stress distributions in 316L stainless steel. Two methods of processing the stresses collected (direct and using a least squares solver) were used. An existing method was used to incorporate the experimental measurements as initial residual stresses; The model results were compared with each other, a model containing no residual stress and the experiment. The least squares method helped remove extreme stresses calculated by the cross-correlation method at points with high mean angular error. The modelled stress distributions from both the direct and least squares model did not fully match the experimentally observed stresses but similarities were seen within some grains.

After loading, little difference was seen between the models, with and without the inclusion of residual stress, implying a negligible effect on the deformation response of the material. However, the predicted stress distribution did not match with the experimentally measured stress distribution after deformation, suggesting further physical effects must be accounted for in crystal plasticity models.

1. Introduction

During the processing and in-service loading conditions of polycrystalline engineering alloys, intragranular stress distributions will always be present due to microstructure determining constraints such as grain boundaries [1]. As they play a significant role in the material's local mechanical response, accurately quantifying and accounting for these residual stresses is critical to predict the development of stress distributions, which is important for understanding meso-scale material deformation and damage that leads to material failure.

For stainless steel, residual stresses are present from early stages of casting, due to grain boundary constraint and inclusions like carbides, which cause geometric incompatibilities. These stresses can be relieved

with post-processing heat treatments, but some residual stress will be still remain [1].

Stresses cannot be directly measured but can be calculated from strains. To quantify stresses, including residual stresses, multiple methods can be employed. There are three distinct stress types: Type-I stress is at the macroscopic scale and captures the grain-averaged stress, applicable to a test sample, or to a component (as a whole, or a particular feature).

There are many methods for measuring type-I residual stress ranging from destructive techniques such as core milling [2–4] and non-destructive techniques like X-ray or neutron diffraction [4–6]. The main issue with these type-I stress measurement techniques is that they do not represent local microstructural changes but rather large

* Corresponding author.

E-mail address: nm20421@bristol.ac.uk (E.W. Horton).

<https://doi.org/10.1016/j.msea.2023.145096>

Received 23 February 2023; Received in revised form 25 April 2023; Accepted 27 April 2023

Available online 2 May 2023

0921-5093/© 2023 The Author(s). Published by Elsevier B.V. This is an open access article under the CC BY license (<http://creativecommons.org/licenses/by/4.0/>).

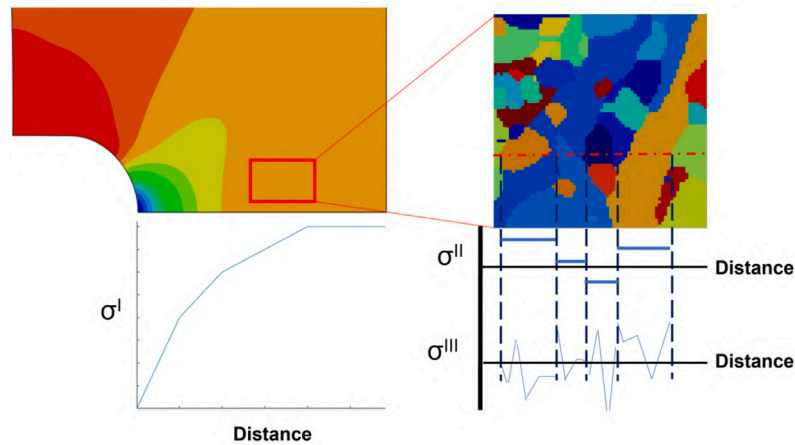


Fig. 1. Stress types classified by the lengthscale. Type-I is macro level stress, Type-II is the mean stress within a grain, and Type-III is the intragranular stress.
Source: Figure reproduced from [14].

differences in stress at a component scale, making them unsuitable for small intragranular stress measurements.

Type-II stress is the mean stress within an individual grain. Previous studies [7–9] using X-ray diffraction (XRD) have captured type-II stresses both before and after loading, allowing the inclusion of stresses before loading in simulations. Both studies found that including these stresses was important to replicate the material's subsequent mechanical response.

Type-III stress is the intragranular stress i.e. the variation of stress within a grain from the mean Type II stress. As this varies from location to location within a grain, the type III stress has a distribution. Their quantification allows for the assessment and influence, at the sub-crystal level, of small microstructural features. Type-III surface stress data can be collected using high resolution electron backscatter diffraction (HR-EBSD), as described in [10–13]. Residual elastic strains, calculated from the measurement of displacements observed in EBSD diffraction patterns are used to infer a stress tensor. This data, comprising of type-III stresses, can be obtained from a single grain, or collected for several grains within a mapped region. Such maps are useful for describing residual intragranular stress maps. A visual representation of the three described stress types is provided in Fig. 1.

Following the measurement of residual stresses to describe an initial deformation condition, this information can be directly incorporated into a model for calculating evolving stress distributions as a function of external loading and microstructure. One method that offers meso-scale modelling capability is crystal plasticity finite element (CPFE).

CPFE has evolved over the past 25 years to become a powerful tool for understanding material behaviour, able to include different physical phenomena. Early implementations by Kalidindi et al. [15] and Beaudoin et al. [16] in the 1990s showed CPFE has the potential to solve deformation and damage problems in many materials. There are numerous examples of successful CPFE implementation for different materials and deformation conditions, e.g. [17–21]. For studies related to deformation, multiple methods for including initial grain-to-grain stress distributions have been proposed.

Musinski [9] incorporated residual stress into crystal plasticity by using an experimentally measured residual stress distribution with respect to depth [22]. The eigenstrains were utilized to impose strains at different depths through the crystal plasticity model geometry. The deformation gradient present in crystal plasticity was split into three components: the usual elastic (F^e) and plastic (F^p) components, and an eigenstrain component (F^0). This eigenstrain deformation gradient was used to include the residual stress in the model by using the linearized form of the green finite-strain tensor. Although this method did not account for high strain rates or elastic wave propagation during shot

peening, promising results were found with good agreement between the experimental and modelling results for initial distributions.

Kapoor et al. [7] proposed another method, which also split the basic crystal plasticity model deformation gradient into three parts: elastic, plastic, and elastic residual. A small strain formulation was used to convert the experimental elastic strains measured using high energy diffraction measurements (HEDM) into deformation gradients, which were directly imported into the model at each integration point. This method works directly with experimental measurements and is similar to the approach used in this study. A more detailed explanation of the methodology is presented in Section 3.3.

Kapoor et al. [14] expanded this work by using experimentally measured geometrically necessary dislocations (GNDs) to simulate residual stress by altering the hardening on different slip systems based on the GND density. This was achieved by calculating the backstress based on the GND density of different slip systems.

This study employs HR-EBSD to capture type-III strain measurements before and after a monotonic uniaxial load, using the method described in [14]. The initial residual elastic strain distribution is incorporated into the crystal plasticity model. Two methods for processing the experimental results are used: one directly imports the strain maps from the HR-EBSD measurements into the crystal plasticity model, while the other runs the stress profiles through a weighted residual stress-based finite element solver. The latter method is employed because type-III stresses only consider intra-granular distributions so the inter-granular stress distributions will not be in equilibrium. This extra step redistributes the stresses to a state closer to equilibrium.

The crystal plasticity model is described in Section 3, and the implementation of [14] is explained in Section 3.3. The implementation of the two residual stress methods into the crystal plasticity solver can be found in Sections 3.4 and 3.5 respectively. This work uses the method proposed by Kapoor et al. [7], as it is the best fit given for the available data.

A comparison between three different modelling approaches with the same geometry and loading conditions is performed with the independent factor being how the residual stresses are included. Model 1 has no initial residual stresses, Model 2 uses the direct residual approach, and Model 3 uses a least squares approach to map the residual stresses initially. These three approaches are compared to the experimental data before and after loading in Section 5. Conclusions are presented in Section 7.

2. Experimental

A sample of grade AISI 316-L stainless steel was ground and polished using a 0.04 μm colloidal silica finishing polish until an appropriate surface quality was obtained. The sample was studied using a Zeiss



Fig. 2. Orientation map of the full HR-EBSD map collected. The orientations shown are displayed relative to the normal direction and colour-coded based on the inverse pole figure included in the figure. (For interpretation of the references to colour in this figure legend, the reader is referred to the web version of this article.)

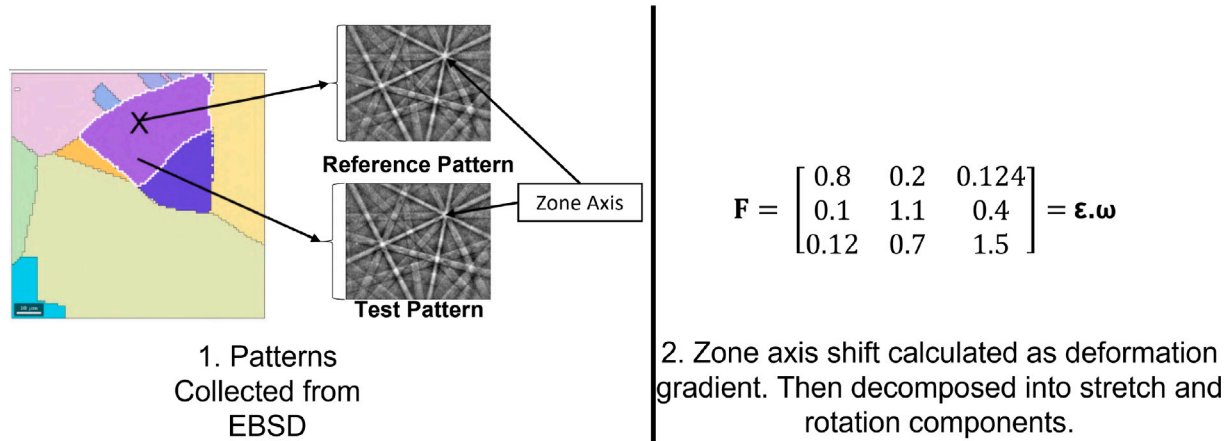


Fig. 3. Diagram representing cross-correlation. The shift of the zone axis between the current pattern and the reference pattern is calculated and represented as a deformation gradient, similar to that seen at the bottom of the figure. From this image it can also be seen that the bandwidth is very thin so this limits the accuracy of the strain measurements possible from the slip band.

Merlin field emission gun scanning electron microscope (FEG-SEM) equipped with a Bruker-eFlash HR-EBSD detector, which was controlled using the Esprit 2.0 software. To keep the sample in place, a small preload of approximately 50 N was applied. The HR-EBSD scan was performed on a chosen area of $440 \times 240 \mu\text{m}^2$ with a step size of $0.5 \mu\text{m}$. The patterns at each point were obtained for analysis. A resolution of $800 \times 600 \text{ pixels}^2$ in 16 bits was chosen for each pattern, providing sufficient angular resolution for offline strain analysis. The probe current and electron beam energy used were 10 nA and 20 keV respectively. Fig. 2 shows the microstructure of the scan in the form of an IPF plot.

After the initial EBSD scan, the sample was loaded to a stress level of 245 MPa at a rate of $6 \times 10^{-5} \text{ s}^{-1}$, resulting in an accumulated strain of 3.7×10^{-3} . The sample was then unloaded and another HR-EBSD scan was performed using the same settings as the first scan.

The patterns from each scan were used to calculate type-III stresses and strains in each grain relative to an assumed zero elastic stress/strain point within the grain using a cross-correlation method described in [11,13,23]. For each grain, a reference point was chosen and its pattern was used as a reference. The location of the zone axis in the reference pattern was compared to the zone axis in every other pattern within the grain and the difference was calculated using a cross-correlation function and outputted as a deformation gradient. This deformation gradient was then decomposed into its symmetric and anti-symmetric parts which represent strains and rotations respectively. Fig. 3 displays this process. The elastic stress was calculated from the elastic strains using the 6 by 6 stiffness matrix (C) as shown in Eq. (1):

$$\sigma = C \cdot \epsilon \quad (1)$$

Due to the reliance on a reference point within a grain to determine stress distributions and no quantifiable way of relating said reference

points to each other, stress profiles within grains cannot be related to stress in other grains. As such only intra-granular (type-III) stress are captured and the inter-granular stresses (type-II) cannot be considered in the following work.

There are two methods to calculate these stresses, each with its limitations. The first method presented by Wilkinson et al. [23], captures all three components of the stress vector but only the deviatoric component. It cannot measure the hydrostatic stress because it is represented by the band width, which cannot be accurately measured due to low resolution of the pattern.

The second method, proposed by Britton et al. [10], increases the maximum lattice rotation to 10° and uses a finite deformation framework for accurate strain calculation, but assumes a zero out-of-plane stress. This method was adopted in the study, as the zero out-of-plane assumption is deemed acceptable due to close proximity of EBSD data collection to the material surface.

Before quality of the data can be assessed areas that contain erroneous stress are identified by considering the misorientation between each EBSD point to the corresponding reference point within each grain. The majority of the grains showed misorientations of less than 0.3° suggesting that the strains maps calculated will be well within the accepted range.

Fig. 4a and b also shows some labelled grains that have misorientations higher than the scale bar. This is caused by the data collection software, ESPRIT 2.0, defining grain boundaries as when the misorientation between adjacent points is greater than 10° which means that grain boundaries that are less than 10° are not defined, leading to ESPRIT combining grains with low misorientation angles. For the purposes of stress calculation via cross-correlation this misidentification of grains creates problems because, the cross-correlation

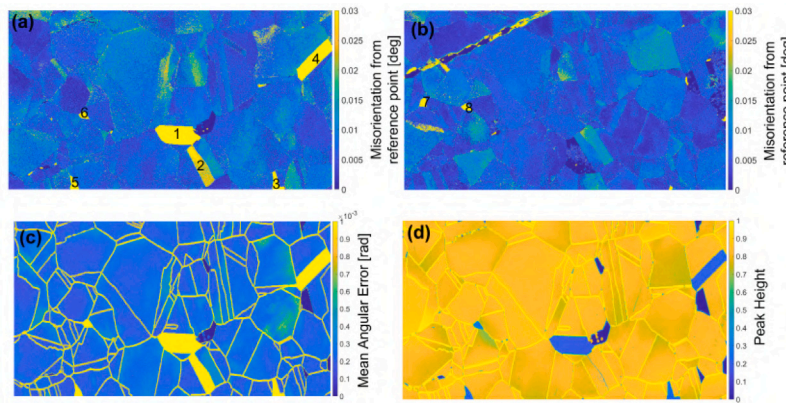


Fig. 4. Various measures of error quantification. (a) and (b) are the misorientation from the reference point of each grain displayed as spatially resolved maps from (a) before and (b) after the test. (c) is the mean angular error and (d) is the peak height from before the test.

software will use the same reference pattern for the incorrectly defined grain as for the grain the reference pattern actually belongs to. This leads to a greater than the 10° difference in the test pattern compared to the reference pattern so the stresses calculated in these regions of high misorientation cannot be accepted with any confidence.

Once the areas containing inaccurate stresses are established the quality of the calculated strains can be assessed by considering at the mean angular error and peak height which are an output of the cross-correlation software. Fig. 4c shows the mean angular error (MAE) which represents how well the shifts and remapping in HR-EBSD fit a deformation gradient. Practically this can be used to indicate the reliability of strain calculations because any value of strain calculated that is less than the MAE may be classed as inaccurate. Fig. 4d shows the peak height which is a direct measure of the correlation between the current point being analysed and the reference point, with a larger peak height indicating better correlation. From these plots it can be seen that the grains showing high misorientation also shown large MAE and low peak height, giving further evidence for stress calculations being unreliable in these regions. The high MAE and high peak heights at the grain boundaries seem to contradict each other but due to the calculated stress profiles displaying unrealistically large stresses at grain boundaries as is shown later in Fig. 5a, the peak height here is ignored in favour for the mean angular error.

For the purposes of this study, the strain distributions that were calculated in these labelled grains are ignored for future comparisons. In the after load map there is also a scratch in the top left of the sample which leads to inaccurate strains. This area is omitted for final comparisons.

3. Crystal plasticity model

The crystal plasticity model used in this study is based on the work of Kalidindi et al. [15], chosen due to its large strain framework, making it more suitable for future use as a predictive tool. The model uses a fully implicit, two-level time integration scheme, which produces reliable results and allows for easier implementation of new constitutive laws compared to a single-level scheme. For a detailed explanation of the time integration scheme, see [15].

To calculate the deformation at each point, the total deformation gradient (F) can be decomposed into its elastic F^e and plastic F^p components, as shown in Eq. (2):

$$F = F^e \cdot F^p \quad (2)$$

This can be rearranged to give Eq. (3):

$$F^e = F \cdot F^{p-1} \quad (3)$$

The total deformation gradient is given by the finite element solver thus only F^p needs to be calculated. The rate of F^p is defined by Eq. (4):

$$\dot{F}^p = L^p F^p \quad (4)$$

where L^p is the velocity gradient and is calculated as follows:

$$L^p = \sum_{\alpha} \dot{\gamma}^{\alpha} (m^{\alpha} \otimes n^{\alpha}), \quad (5)$$

Here, $\dot{\gamma}^{\alpha}$ is the shearing rate in a slip system α , m^{α} is the slip plane normal and n^{α} is the slip direction.

3.1. Constitutive laws

The slip rate law used is shown by Eq. (6) and detailed in [24].

$$\dot{\gamma}^{\alpha} = \dot{\gamma}_0 \left(\frac{|\tau^{\alpha} - X^{\alpha}|}{g^{\alpha}} \right)^{\frac{1}{m}} \text{sgn}(\tau^{\alpha} - X^{\alpha}) \quad (6)$$

where $\dot{\gamma}_0$ and m are the reference slip rate and the rate exponent for slip and τ^{α} is the resolved shear stress.

Backstress is included in the slip rate law to incorporate intragranular residual stresses caused by obstacles to dislocation motion such as grain boundaries. This phenomenological approach has been used by several researchers [25–27] and is deemed useful for this work due to the intra-granular nature of the stresses captured by cross-correlation of HR-EBSD patterns.

The backstress (X) is described by the Armstrong and Frederick Model [28], as shown in Eq. (7),

$$\dot{X}^{\alpha} = h \dot{\gamma}^{\alpha} - h_D X^{\alpha} | \dot{\gamma}^{\alpha} | \quad (7)$$

where h is the hardening term and h_D is the softening term. The slip system hardening evolves according to Eq. (8),

$$\dot{g}^{\alpha} = \sum_{\beta=1}^N H^{\alpha\beta} \dot{g}^{\beta} \quad (8)$$

where $H^{\alpha\beta}$ is the hardening matrix which is constructed using the latent hardening coefficient, q , as in Eq. (9).

$$H^{\alpha\beta} = \begin{bmatrix} 1 & q1 & q1 & q1 \\ q1 & 1 & q1 & q1 \\ q1 & q1 & 1 & q1 \\ q1 & q1 & q1 & 1 \end{bmatrix} \quad (9)$$

Previous studies [29,30] have shown that the values of q for experimental work fall between 1.0 and 1.4. A value of 1.2 was chosen to both fall within this range, and also allows for comparison with the work from [24] which used $q = 1.2$. In Eq. (9) $\mathbf{1}$ is not the identity matrix, but a 3×3 matrix consisting of ones.

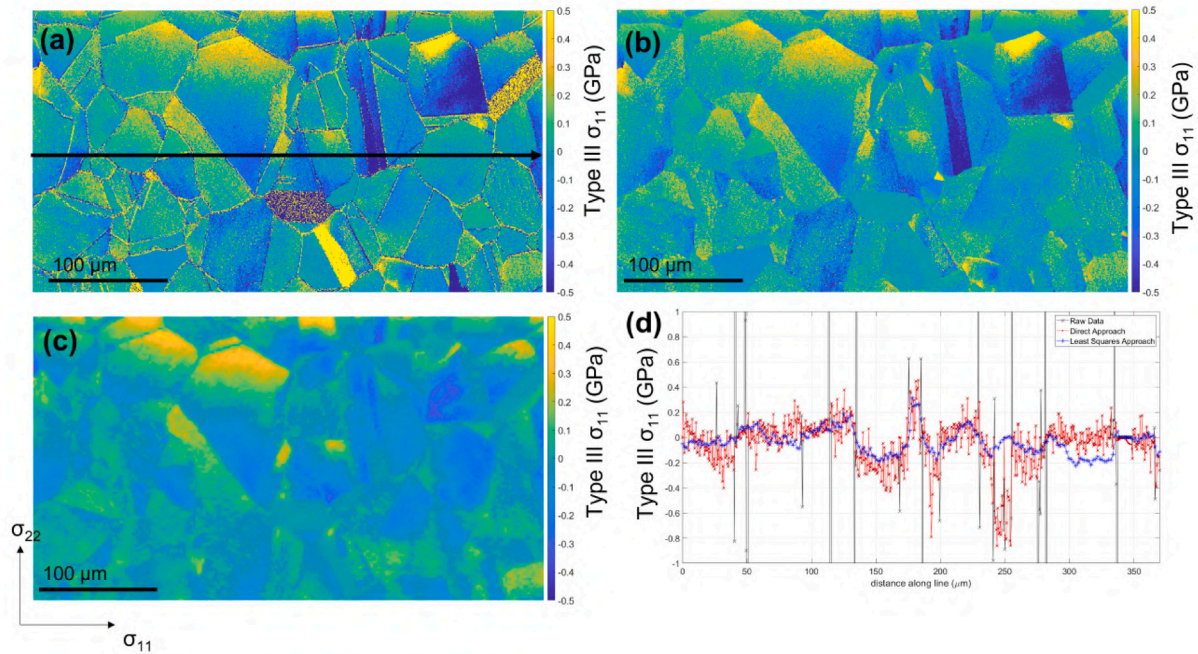


Fig. 5. Experimental Type-III stress maps in the loading direction, σ_{11} from before deformation occurs. (a) A map in the unprocessed data, and (b) shows the map after the processing steps described in Section 3.4. (c) represents the stress contours produced after the least squares method has been applied. (d) a line profile along the black line in (a). This line profile contains the stress profiles from the raw data set (black), the direct approach (red) and the least squares approach (blue). (For interpretation of the references to colour in this figure legend, the reader is referred to the web version of this article.)

The Self-hardening rate, \dot{g}^α , on each slip system is given by Eq. (10). The left-hand-side term stands for strain hardening in which h_0 and n are the parameters for the rate and the exponent. The term on the right-hand-side represents the thermal softening in which A , d , and Q are the softening parameters, R is the universal gas constant and T is the absolute temperature [31].

$$\dot{g}^\alpha = h_0 \left(1 + \frac{h_0 \Gamma}{g^\alpha n} \right)^{n-1} - A (g^\alpha)^d \exp \left(\frac{-Q}{RT} \right) \quad (10)$$

The total accumulated shear strain of all slip systems (Γ) is computed in Eq. (11).

$$\Gamma = \sum_{\alpha} \int_0^t |\dot{\gamma}^\alpha| dt \quad (11)$$

where t is time. This model was selected because previous analysis of a similar experiment on the same material was performed using the same constitutive laws, which enables comparison of results in this paper with those presented in Ref. [24].

3.2. Grain size effect

It has been shown that the yield strength of a grain is inversely proportional to its size [32]. To include this effect in the model, a micro Hall–Petch formulation developed by Agius et al. is used. The reader is referred to Appendix or the corresponding paper [24] for further details.

3.3. Residual stresses

It is well documented [7,9,14] that the initial conditions, including residual stresses, need to be carefully controlled to match the stresses seen in experimental work. One such condition is the presence of stresses before the experimental took place, for ease of reading, this will be referred to as residual stresses from now on.

Previous studies [7,14] have incorporated pre-simulation stress distributions into the above model by decomposing the total deformation

gradient into elastic (F^e), residual (F^r) and plastic (F^p) components, as shown in Eq. (12).

$$F = F^e F^r F^p \quad (12)$$

These residual stresses are present in the undeformed microstructure so these stresses should not cause any deformation of the initial mesh. This can be represented by stating that the total deformation gradient is equal to the identity tensor when applying these residual stresses, as shown in Eq. (13).

$$F = F^e F^r F^p = I \quad (13)$$

Within the CP framework used the most practical way of ensuring Eq. (13) is satisfied is to define F^e as the inverse of F^r , Eq. (14).

$$F^e = (F^r)^{-1} \quad (14)$$

As mentioned by Kapoor et al. [7] it can be argued that this is a physically sound implementation because the residual stresses calculated from HR-EBSD are the elastic response to previous plastic deformation justifying why F^e is modified and F^p is left as the I .

F^r is calculated at every integration point by external scripts outlined in Sections 3.4 and 3.5 and then introduced into the CPFE model using an input file.

To calculate the residual stresses present before the material was loaded, two different methods were used. These methods calculated the residual deformation gradient F^r from the experimentally measured stress and strain maps using the pattern cross-correlation procedure described in Section 2. A description of the two methods can be found below in Sections 3.4 and 3.5.

3.4. Adding residual stresses: Direct approach

To calculate the residual stresses present before the material was loaded, the elastic strains found using the method outlined in Section 2 from the pre-load EBSD map, ϵ^e , were converted into deformation gradients using the small strain formulation, Eq. (15).

$$F^e \approx \epsilon^e + I \quad (15)$$

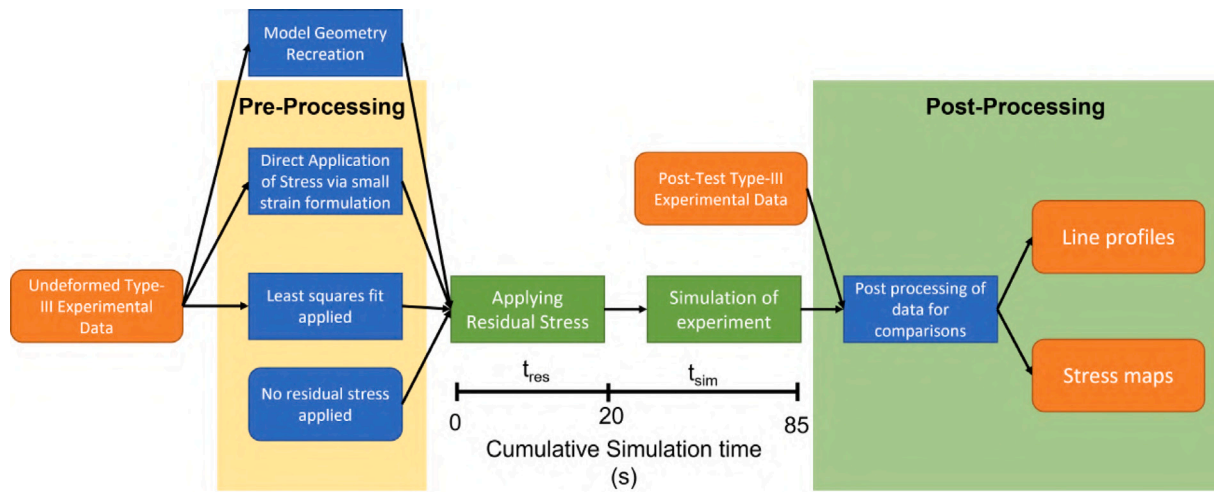


Fig. 6. Flowchart showing the key stages of the procedure devised in this study.

Before the strains could be calculated using this method some simple cleanup routines were performed on the data. Fig. 5a shows the stress map in the loading direction without any processing on it. The contour map in Fig. 5a is limited to ± 0.5 GPa so that the intra-granular stresses are clearly visible, however the stresses along grain boundaries frequently exceed 10 GPa. This is deemed to be a measurement error because the boundaries often have very high MAE (see Fig. 4). Other grains also contain large MAE and have consistently high stresses throughout them.

To remove these unreliable stress values that are evident in Fig. 5a the MAE was considered at each point within the map. If the MAE exceeded 6×10^{-4} then any value of stress and strain was removed from the dataset and initially replaced with NaN. A value of 6×10^{-4} was selected as the maximum acceptable MAE because this value removed the extreme stresses without impacting values within an acceptable stress range. A second processing step was subsequently applied in which every point containing a NaN value was set to an average of the surrounding elements that were in the same grain as the NaN point. Fig. 5b shows the resulting map. It can clearly be seen that the extreme residual stresses present have been removed. Further confirmation of the effect of the initial processing steps can be seen in Fig. 5d which shows a line profile through the centre of the map. It is clear that the grain boundaries no longer contain extreme stress values.

3.5. Adding residual stresses: Least squares fit with physical constraints

One potential problem with the direct method described in Section 3.4 is that the stresses from the HR-EBSD are type III stresses [33] so there is no inter-granular equilibrium. Whilst an effort is made to reach equilibrium in the initial residual stress input step (see Section 3.3) by allocating extra time for the stresses to redistribute, more pre-processing may be done to move the distributions further towards an equilibrium state. The direct method also shows significant noise within grains which may not represent the actual type-III stress at these locations. To counter the problems present in the direct method an additional pre-processing step was added to help re-distribute these stress distributions more effectively.

In this procedure another stress based finite element method was applied that used the stress components as the field variables, $\sigma(\mathbf{x})$, as a function of the position \mathbf{x} , Eq. (16).

$$\sigma(\mathbf{x})^T = \{\sigma_{11} \quad \sigma_{22} \quad \sigma_{12}\} \quad (16)$$

Only the in-plane stresses are considered in this solver because the experimental data assumes a zero out-of-plane stress (σ_{33}) so the stress profiles with any out-of-plane components are disregarded.

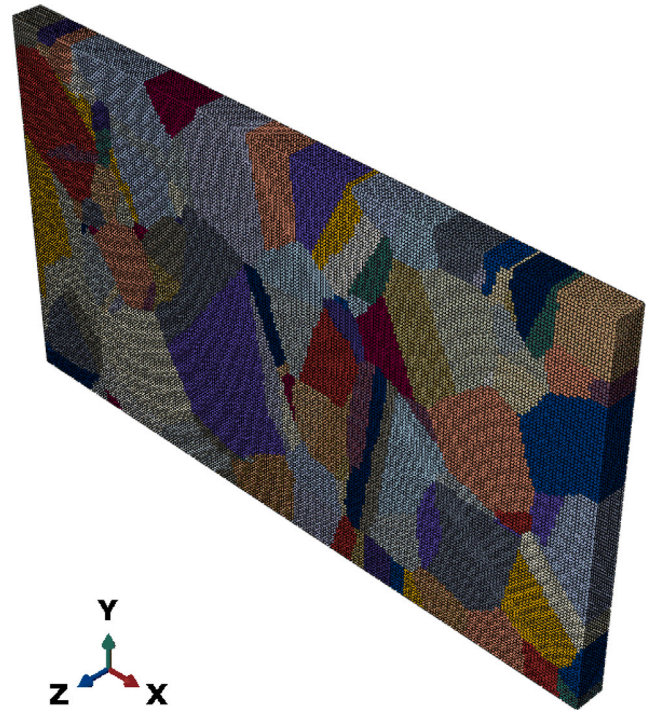


Fig. 7. Mesh created by Dream3D to replicate the microstructure measured by EBSD. The model contained 136 grains and a mesh with 260,400 elements, 10 layers thick.

The important features of this method are highlighted in the following;

- Least squares to match experimental data as best as possible
- Divergence of the stress field to enforce local stress states at equilibrium
- Traction-free grain boundaries to minimize unrealistic stresses near the grain boundaries

The local residual – the difference between the experimental measurements, σ_{exp} , and the field, $\sigma(\mathbf{x})$ – is minimized by setting it zero through Eq. (17).

$$\sigma(\mathbf{x}) - \sigma_{exp} = 0 \quad (17)$$

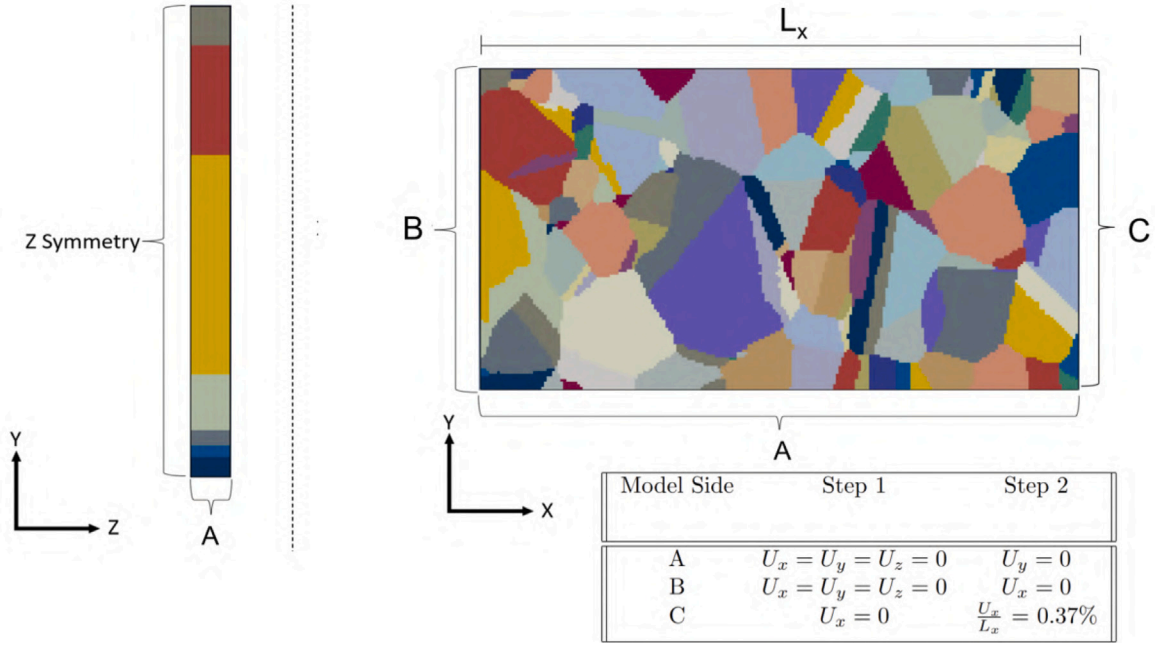


Fig. 8. Boundary conditions used throughout experiment. Step 1 refers to the step in which the residual stresses are applied. Step 2 refers to the step involving simulation of the test.

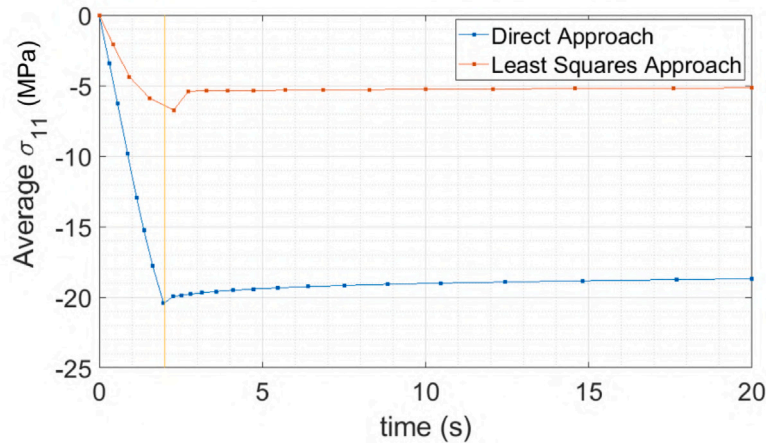


Fig. 9. Average stress in the loading direction over the whole mesh during the application of the residual stresses. The vertical yellow line indicates when the residual stress is fully applied. A time of 18 s was chosen because by this time both methods of including residual stress had reached equilibrium. (For interpretation of the references to colour in this figure legend, the reader is referred to the web version of this article.)

Discretizing the stress field using interpolation functions, $\mathbf{N}(\mathbf{x})$, together with nodal values of stresses, $\tilde{\sigma}$, gives Eq. (18).

$$\sigma(\mathbf{x}) = \mathbf{N}(\mathbf{x}) \tilde{\sigma} \quad (18)$$

Multiplication with the weight function, $\psi(\mathbf{x})$, that is followed by integration of the residual over domain Ω reveals the weak form as in Eq. (19).

$$\int_{\Omega} \psi(\mathbf{x}) [\mathbf{N}(\mathbf{x}) \tilde{\sigma} - \sigma_{exp}] d\Omega = 0 \quad (19)$$

Using the interpolation function as the weight function gives a mass matrix, \mathbf{M} , and force-like vector, \mathbf{q} , that is constructed from the given stresses,.

$$[\mathbf{M}] \{\tilde{\sigma}\} = \{\mathbf{q}\} \quad (20)$$

in which $[\mathbf{M}]$ and $\{\mathbf{q}\}$ are computed using Eqs. (21) and (22).

$$\{\mathbf{M}\} = \int_{\Omega} [\mathbf{N}]^T [\mathbf{N}] d\Omega \quad (21)$$

$$\{\mathbf{q}\} = \int_{\Omega} [\mathbf{N}]^T \{\sigma_{exp}\} d\Omega \quad (22)$$

Similarly, the equilibrium constraint is computed by application of the same procedure to the local divergence equation ($\nabla \cdot \sigma = 0$) giving Eq. (23) in which $[\mathbf{K}]$ represents the divergence operator that is constructed using the derivatives of interpolation functions with appropriate order. The details of the procedure can also be found in the Refs. [34–36].

$$[\mathbf{K}] \{\tilde{\sigma}\} = \{\mathbf{0}\} \quad (23)$$

Grain boundary tractions are set to zero as an additional physical constraint at the micro scale. To achieve that, the element surfaces in 3D (element edges in 2D) that define a grain boundary are identified and local tractions are set to zero giving Eq. (24).

$$\sigma(\mathbf{x}) \cdot \mathbf{r}(\mathbf{x}) = 0 \quad (24)$$

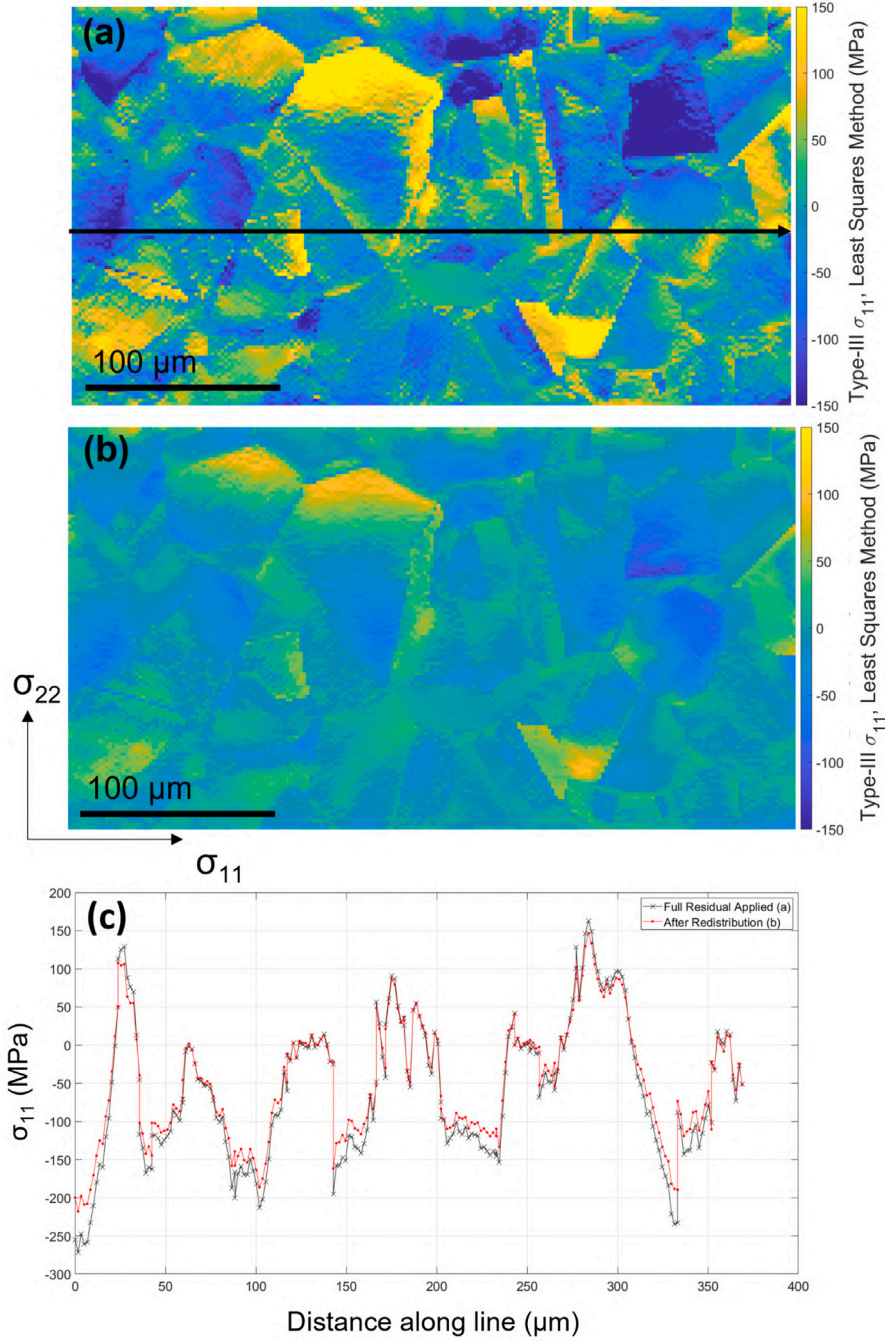


Fig. 10. Displays the full maps from the least squares approach of type-III stress in the loading direction at (a) 2 s (Just after the full residual stress is applied) and (b) 20 s (after the system is left to redistribute). (c) depicts a line profile through maps (a) and (b). Stress redistribution over this time is seen in both methods.

or,

$$[\mathbf{T}] \cdot \{\sigma(\mathbf{x})\} = \{\mathbf{0}\} \quad (25)$$

$[\mathbf{T}]$ is the traction operator to compute the traction from stress components as in Eq. (25). Eq. (26) defines the traction operator, $[\mathbf{T}]$, for the edge normal of an element vector in 2D, \mathbf{r} , with components of r_x and r_y .

$$[\mathbf{T}] = \begin{bmatrix} r_x & 0 & r_y \\ 0 & r_y & r_x \end{bmatrix} \quad (26)$$

$[\mathbf{L}]$ represents the traction-free edge constraint with the edge interpolation functions, $[\mathbf{N}_e]$, over the edges of the domain, ω , as shown in

Eq. (27).

$$[\mathbf{L}] = \int_{\omega} [\mathbf{R}]^T [\mathbf{N}_e]^T [\mathbf{N}_e] [\mathbf{R}] d\omega \quad (27)$$

The overall constraint on the stresses takes the form in Eq. (28) in which κ and λ represent the penalty factors that are used to enforce equilibrium and traction-free grain boundary constraints, respectively.

$$(\kappa[\mathbf{K}] + \lambda[\mathbf{L}] + [\mathbf{M}]) \{\tilde{\sigma}\} = \{\mathbf{q}\} \quad (28)$$

The distribution of stresses, $\{\tilde{\sigma}\}$, obtained by this method were later used to compute the stresses at the integration points of the elements. These stresses were then transformed to the crystal reference frame and subsequently single crystal compliance was used to compute back

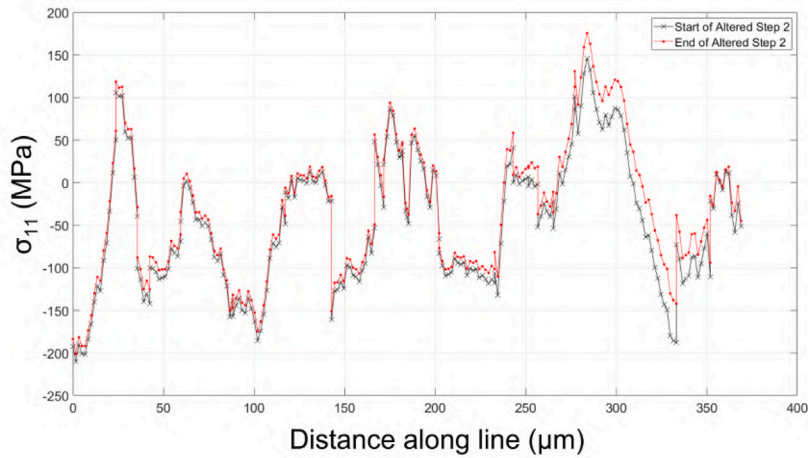


Fig. 11. Type-III σ_{11} line profiles from the Least Squares approach starting at the beginning of the altered step 2 (black) and after 60 s (red). (For interpretation of the references to colour in this figure legend, the reader is referred to the web version of this article.)

the elastic strains in the crystal reference, E^e . The same procedure as described to incorporate these initial elastic strains as residual deformation was used as explained earlier. The stress profile created is visible in Fig. 5c and d. From this figure set it is evident that the least squares method maintains the general distribution of stresses in the majority of grains whilst smoothing out the noise from the experiments. Regions with sudden deviation from neighbouring points, such as 240–250 μm along the line, are less well represented due to the least square method forcing equilibrium across the whole mesh.

4. Crystal plasticity model creation and boundary conditions

The modelling procedure developed is shown in Fig. 6; the flowchart describes the key stages of the study from the start (experimental data collection) to the final post-processing (result comparisons).

4.1. EBSD reconstruction

This section comprises the ‘Model Geometry Recreation’ within the flowchart in Fig. 6.

In an endeavour to replicate the stress distributions obtained from the experiment described in Section 2, the microstructural reconstruction software, Dream3D [37], was used to produce a finite element mesh to replicate the grain morphology and orientations measured via EBSD. Initially, a single layer of elements was used but this proved to not accurately represent the material behaviour. To remedy this the single layer of elements was stacked on top of itself 10 times to create an oligocrystal. The final structure can be seen in Fig. 7.

The mesh created by Dream3D had 260,400 solid brick (C3D8) elements and contained 136 grains. This mesh size allowed every grain to contain at least four elements per layer whilst not using excessive computational resources.

The EBSD measurements of the undeformed sample microstructure were used to create an Abaqus[®] mesh directly. Upon creating the mesh Abaqus[®] CAE was used to add physically realistic boundary conditions to the geometry. These change throughout the course of the simulation so the boundary conditions for each step will be set out separately.

4.2. Residual stress initiation

This section describes the boundary conditions used in the ‘Applying Residual Stress’ section of the flowchart in Fig. 6.

In reality residual stresses already exist within the material but in the model they have to be initialized. To do this an extra step

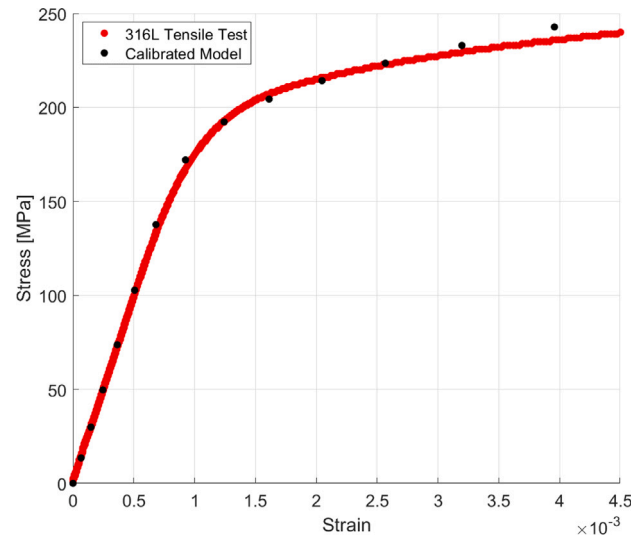


Fig. 12. Loading curves from a tensile test of 316L under similar conditions (Red) and the model after calibration (Black). (For interpretation of the references to colour in this figure legend, the reader is referred to the web version of this article.)

was included before loading so that the residual stresses calculated in Sections 3.4 or 3.5 can be implemented. The stresses were then implemented by applying the calculated stress field linearly over a set time period which ensured convergence. Once the stress field was fully applied the boundary conditions used in this step, that are described below, were preserved until the stress field rearranged itself into a stable configuration. When stress averaged over every element stops fluctuating, this is defined as the stable configuration.

The time to reach this stable state was found by running another simulation with only the residual step simulated. The stress in the loading direction was then taken from every integration point and averaged at each time step and plotted, as seen in Fig. 9. The least squares approach reaches equilibrium much faster than the direct approach. This is expected because processing of the former is already complete, thus the simulation starts closer to equilibrium. This figure also highlights the strength of the least squares method because the larger average stress magnitude seen in the direct approach is caused by the large stress peaks present due to incorrectly calculated strains from badly correlated peaks. These peaks are smoothed out by the least squares method making for a lower average stress.

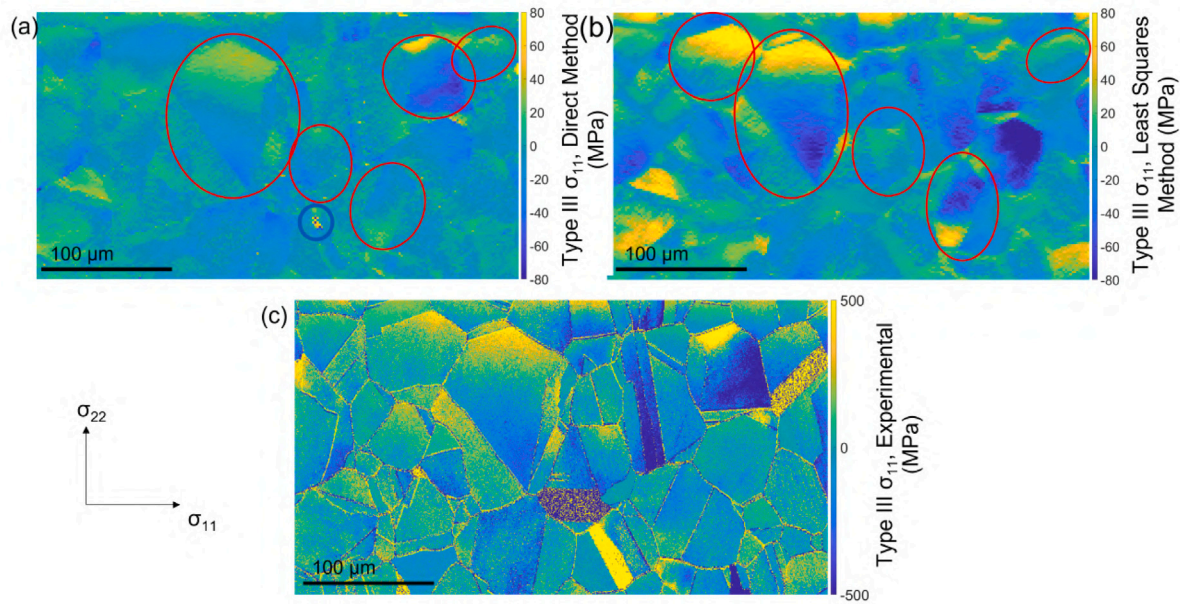


Fig. 13. Three maps comparing the type-III stress in the loading direction from (a) the direct method, (b) the least squares method and (c) the experimental results before any load is applied. The red circles indicate areas in which the stress distributions match with the experimentally measured data (c). The blue circle in (a) highlights an area of extreme stress. (For interpretation of the references to colour in this figure legend, the reader is referred to the web version of this article.)

The boundary conditions impose a constraint that mimics the surrounding microstructure, outside of the simulated volume, so any internal forces within the material do not distort the shape of the simulated volume. This condition was applied in all three primary directions because the stresses applied during the residual step are already present within the simulated volume; no distortion of the mesh is permitted.

The CP formulation itself stops the residual stresses from causing deformation, as described in Section 3.3, but to ensure this occurs a pinning constraint ($U_x = U_y = U_z = 0$) is applied as a boundary condition on side A and B of the mesh (See Fig. 8) and a zero displacement boundary condition is present on side C. The reader is referred to Fig. 8 for the implementation onto the FE mesh described in Section 4.1.

A z-symmetry condition was applied to the plane normal to the z direction that would be within the material, as labelled on Fig. 8. This allows stresses to redistribute into the volume of a grain that was not modelled i.e. for the unknown subsurface microstructure.

Fig. 10 shows the difference in the stress distributions between immediately after the residual deformations were fully applied and at the end of the residual step. Some relaxation is evident, although the locations of stress peaks and troughs remain similar. This map and all the remaining figures that display the overall stress distribution have data presented from the free surface (normal to the z direction), representing the surface of the material which can be directly compared to the experimental EBSD measurements.

4.3. Loading stage

Once the residual stress was applied, the second simulation section of the flowchart in Fig. 6 began and the simulation was now ready to model the experiment outlined in Section 2. During this step, the boundary conditions applied were changed to those shown in Fig. 8 under Step 2. Side A and B in Fig. 8 were constrained so that they were not able to move in the direction of their plane normals, representing the surrounding microstructure inhibiting movement in these directions.

The redistribution of stresses caused by the change in boundary conditions was investigated by running a separate simulation in which the boundary condition present on side C during step 2 was omitted.

This allowed for the stresses to redistribute without any effect of load. Fig. 11 shows a line profile from along the same line present in Fig. 10. Minimal stress redistribution is seen indicating this change in boundary conditions does not significantly change the behaviour.

To simulate the experimental loading conditions, a displacement boundary condition was applied uniformly over side C in Fig. 8 corresponding to a final macroscopic strain of 0.37% occurring in the positive x direction. This strain magnitude was used because it matched the experiment strain. Once the allocated strain was reached the displacement boundary condition was removed and the simulation was given time to fully unload. The boundary conditions applied are described in Fig. 8 under Step 2.

4.4. Calibration

To help the crystal plasticity model, described in Section 3, better predict the mechanical behaviour observed experimentally, the average stress-strain response of the geometry seen in Fig. 7 was compared against a macroscopic tensile test. The experimental curve used was taken from a tensile test of the same material cast in the same conditions.

The boundary conditions applied to the model geometry were the same as those presented in Fig. 8, Step 2, with one notable difference comprising of increasing the total strain applied to 0.5%. Fig. 12 shows the experimentally measured loading curve used for calibration, and the calibrated model simulation loading curve.

The authors acknowledge that the experimental data used for calibration will have an initial residual stress field, however this is not considered within this paper because the goal of this work is to identify the effect of including residual stress. As such establishing a mechanical response that is not influenced by residual stress is necessary for later comparisons where residual stress is considered.

An initial value for every variable was taken from [24] because these variables were used to simulate the same material with the same constitutive laws and length scale model used here. In this study, manual calibration was done to fit the modelled results to the experimental data by changing the hardening rate (h_0) and reference slip rate ($\dot{\gamma}_0$). Values were chosen to match the initial slip rate; this was judged

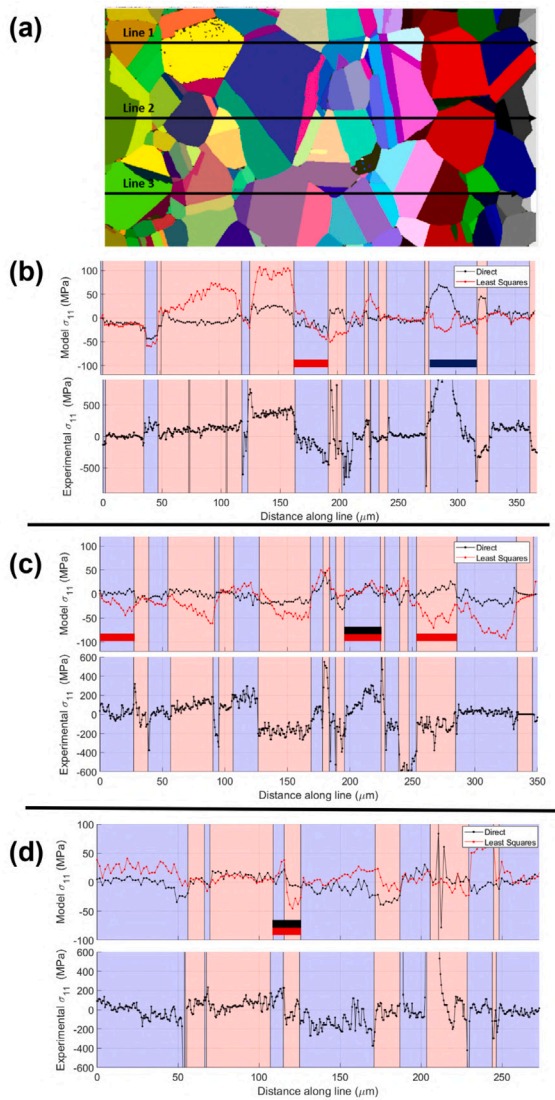


Fig. 14. Type-III, loading direction (σ_{11}) stress distributions before loading taken along the lines shown in (a). (b) Line 1, (c) Line 2, (d) Line 3. The blue and red background colours represent grains in the material. The black and red boxes indicate grains which generally follow the same trend as the experimental profiles. Black = Direct approach, Red = Least squares approach. (For interpretation of the references to colour in this figure legend, the reader is referred to the web version of this article.)

Table 1
Model parameters used.

Parameter	Value	Unit
C_{11}	250 000	MPa
C_{22}	145 700	MPa
C_{44}	130 600	MPa
$\dot{\gamma}_0$	0.0001	–
m	0.05	–
g_0^*	75	MPa
h_0	100	MPa
n	0.14	–
Q	418 000	kJ mol^{-1}
d	3	–
A	0	–
h	6555	MPa
h_D	245	–
k	6.8	MPa mm
c	0.24	–
q	1.2	–

as a key process for accurate simulation of the stress distributions that achieved numerical convergence. Parameters for length scale and kinematic hardening were obtained from Agius et al. [31] for this material. Table 1 shows the final parameters used.

4.5. Models run

To understand the effect of including residual stresses, 3 simulations were performed:

1. A model with no initial residual stress included.
2. A model with the residual stresses included, as calculated by the direct approach (Section 3.4).
3. A model with the residual stresses included, as calculated using the least squares approach described in Section 3.5.

5. Results

To fully utilize the data obtained, two comparisons are performed. The first examines the results of the direct and least squares models by examining the residual stress in each grain before any loading takes place. These results are bench-marked against the experimentally measured residual elastic stresses from the HR-EBSD method of the material in the undeformed state are used. The second is a comparison of the three models outlined in Section 4.5 after the experimental loading has been applied. The resultant stresses after deformation, in the unloaded state, are compared to the residual elastic stresses obtained via the HR-EBSD scan of the sample in the post-test condition. As mentioned in Section 2 only in-plane stresses are considered because the HR-EBSD method assumes there are no out-of-plane stresses. This assumption ($\sigma_{33} = 0$) is made so that hydrostatic stresses can be included in the stress components. For further details about the scientific basis on this please see [10].

For the crystal plasticity model, both type-II and type-III stresses are calculated. As the HR-EBSD method can only measure type III stresses, the type-II stresses in the model must be subtracted for a direct comparison. This was done by using the stress free points for each grain taken from the experimental work and subtracting the model stress from this point for every other point within that grain. The same process was performed with the strain matrices as well. This falls in the post processing section of Fig. 6's flowchart.

5.1. Prior to loading

Fig. 13 compares the type-III stress before loading in the loading direction (σ_{11}) of the two methods (Fig. 13a,b) used to incorporate residual stresses as well as the corresponding experimental stress map, Fig. 13(c). Before comparison, it is noted that the stress magnitude plotted in the experimental maps is significantly larger than those shown for the modelled results. This is necessary because if the range is made the same in the experimental plots as the simulated plots, little comparison can be made. For this reason, comparisons will only be qualitative.

When comparing the two simulated maps to the experimental map qualitative similarities in stress distribution can be seen. These areas are highlighted in red. The locations of the red circles on the maps do not always appear in the same locations on both maps so a difference between the two approaches is apparent. One of the most noticeable differences between the two models is the broader distribution of stresses calculated by the least squares method. It is also worth noting the least squares method does not contain any extreme stress discontinuities, unlike the direct method. The blue circle in Fig. 13a indicates the location of these extreme stresses.

To further compare the type III stresses between the model and experiment, stresses have been extracted from the maps, across several grains, along the three lines shown in Fig. 14a. Fig. 14b–d shows the

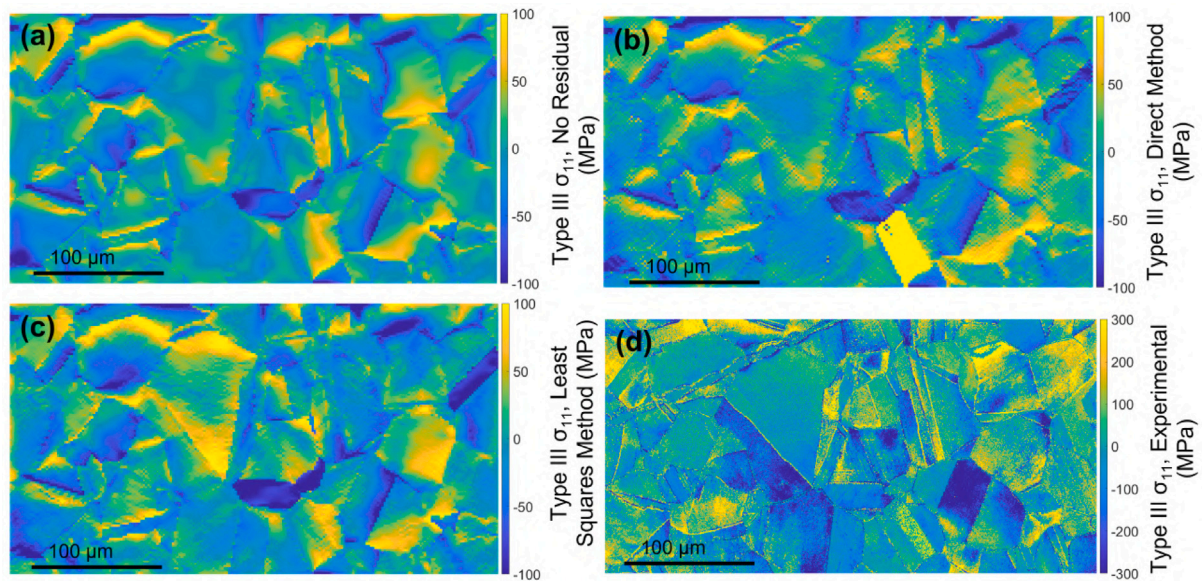


Fig. 15. Type-III stress in the loading direction (σ_{11}) at the end of the simulation. (a) is the sim with no residual stresses, (b) uses the direct method, (c) uses the least squares method and (d) is the experimental data.

three profiles with the stress distributions; the alternating blue and red coloured areas represent different grains. As can be seen from these plots, whilst the simulated stress distributions from both models do not fully line up with those stresses seen experimentally there are still some areas which bear some similarities. A few grains show similar distributions to the experimental results, indicated by the red and black boxes in Fig. 14, which matches with the qualitative analysis of Fig. 13 but in general the distributions do not match.

5.2. Post loading

Fig. 15 compares the distribution of stress in the loading direction obtained from the model, with no residual stress (Fig. 15a), with directly imported residual stress (Fig. 15b), with least squares calculated residual stress (Fig. 15c) and experimental results (Fig. 15d). A large scratch can be seen on the surface in the top left corner of the experimental data so this must be taken into account when comparing stress maps.

From Fig. 15 it is apparent that the stress distributions calculated after loading from the different residual stress methods are very similar. The least squares method shows the most broad distribution of stress, most likely due to the presence of the highest magnitude initial residual stress distributions. None of the simulated maps replicate the experimental measured distributions seen in Fig. 15d.

For a further comparison between the simulated and the measured results, line profiles were once again extracted from the datasets, as shown in Fig. 16a. Note that line 1 does not extend across the EBSD map to avoid a scratch in the sample surface. This scratch was created at an unknown time after the initial EBSD map was collected hence why it only appears in the post-loading maps. Fig. 16b,c and d shows the type-III stress in the loading direction along the three line profiles. The stress distributions per grain are once again identified by the blue and red coloured areas. When the stresses produced by the models are compared to each other, the same trend can be seen between the three approaches. The least squares approach offers the largest difference in stress distribution from the model with no residual stresses. When comparing the experimental results with the modelling results a large difference in stress distributions is evident both in the line profiles of Fig. 16 and the stress maps of Fig. 15.

With all three simulated maps showing a similar final distribution after different initial stress fields, the time at which the distributions

converged is of interest. To find this a line profile taken along line 2 from Fig. 16d was extracted at 0%, 0.05%, 0.12% and 0.2% strain. Fig. 17 displays the stress profiles from all three simulated models.

From 0.05% strain a reduction in the magnitude of the peaks seen in the residual stress models is visible such as the peaks at 80, 180, 260 and 280 μm . This trend continues as the strain increases. 0.05% strain also marks the strain at which the intragranular distributions begin to distort so that they follow the trends set by the model with no residual stress. This is particularly clear in the first grain (0–25 μm) for both models and in the grain between 200 and 235 μm in the least squares model. This suggests even from the initial instance of loading, the residual stresses begin to be redistributed, with larger loading stresses pushing the initialized residual stresses closer to the distribution with no residual stresses. Once 0.2% strain is reached the initial residual stress distributions added have disappeared in a significant number of grains.

Another avenue allowing for the effect of the initial residual stress to be observed involves comparing the stress–strain curves produced by each simulation. To achieve this the average stress and strain from the whole geometry was extracted.

The stress–strain curves were subsequently shifted to ensure that begin loading the stress and strain were 0. This allowed a comparison of the behaviour with the assumption that there was no knowledge of the stress profiles prior to loading. Fig. 18 shows the loading curves produced by the three simulations.

The least squares and direct approach reach higher total stresses than the simulation containing no initial residual stress due to the initial stress distributions adding a plastic strain prior to loading, however the magnitude of the difference between the curves remains similar to that seen when comparing intra-granular stresses. This further backs up the conclusion that whilst the addition of residual stress does have some effect on the average mechanical response, it is minimal.

6. Discussion

The initial type-III residual stresses, measured using cross-correlation of HR-EBSD patterns, were shown to create a stress field within the material but ultimately disappeared upon loading to 0.37% strain. The lack of noticeable changes in the post-test stress fields could be due to the lack of type-II residual stresses which are not possible to collect with the strain measurement method applied.

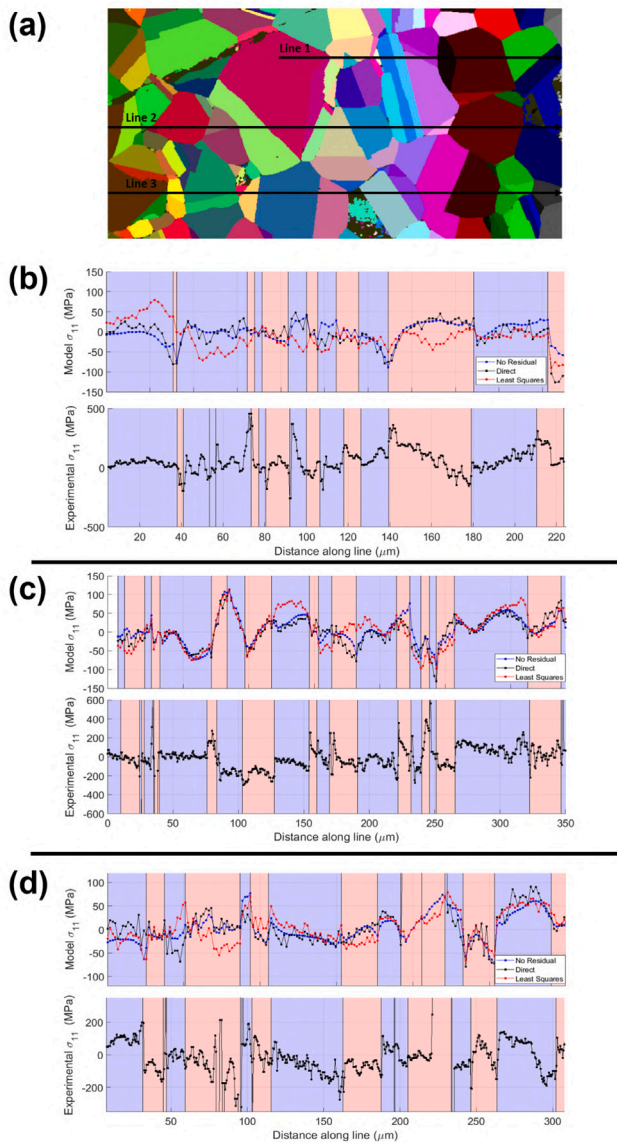


Fig. 16. Type-III stress in the loading direction along line profiles depicted in (a). (b) follows line 1, (c) line 2 and (d) line 3. (For interpretation of the references to colour in this figure legend, the reader is referred to the web version of this article.)

The use of the least squares pre-processing was an attempt to help the stress profile reach an equilibrium state but this method was designed to push intragranular stress distribution within grains to equilibrium without changing the intergranular stress state. This, therefore, does not address potential problems involving type-II stresses. The importance of Type-II stresses has been shown in previous work performed by Kapoor et al. [7], which demonstrated that including the type-II stresses in a crystal plasticity simulation significantly improved the match between experimental and model results in a titanium alloy. However this work required the utilization of far field synchrotron XRD to gather the strains, a complex and time consuming method.

Far field 3D XRD is a well used method for obtaining through-thickness Type-II stress measurements within a material but this does not allow for the capturing exact grain morphology but rather just the centre of mass of a grain. 3D XRD can be used to capture grain morphology but a near field approach, such as that used by Turner et al. [1], is needed and this does not allow for strain measurements. A combination of the two methodologies such as the work by Turner et al. [1] has proved to be possible but is not a simple procedure,

unlike the EBSD measurements used in this work which are considered routine. Other additional processes exist that can be used alongside XRD, such as diffraction contrast tomography (DCT), but these still have limited resolution so for materials with smaller grains, such as the stainless steel looked at in this work, not every grain would be captured by this method.

Another possible reason for the dissimilar stress distributions seen between the models and the experiment could be due to the sub-surface microstructure and corresponding stress fields being ignored. This ties into the lack of Type-II stresses because sub-surface grains would also contain Type-II and III stress fields that would affect the grains visible on the surface. A logical future step would be to obtain a 3D microstructure, and use this data for simulations, but such experiments are highly specialized and time consuming.

3D EBSD is one possible way of obtaining high resolution 3D microstructural geometries but this method is destructive so making in-situ loading or pre-test 3D stress measurements impossible. 3D EBSD also does not allow the collection of residual stress measurements using the cross-correlation approach used in this paper because this approach assumes a plane stress (surface) condition so any out-of-plane stresses, which would certainly be present sub-surface, are not taken into account.

In recent years, scanning 3DXRD has been introduced into a few of facilities worldwide, enabling the measurement of Type-II and Type-III stresses in a 3D volume. The results produced by Hayashi [38] look promising for capturing 3D stresses, but the prohibitive difficulty of performing these experiments makes them expensive and time consuming. If this technique becomes more widespread, the stress fields measured could be implemented into the crystal plasticity model presented here using the current formulation for including residual stresses. This could potentially improve the predictive capabilities of the model by allowing the correct implementation of initial conditions seen within the microstructure in three dimensions.

Whilst neither the direct or least squares approach demonstrated similar stress distributions to those seen experimentally, the two methods did display some differences in distributions upon initialization. One possible reason for this is the different approaches applied to grain boundaries. The direct method takes the exact Type-III stress fields measured which are influenced by the Type-II stresses that are present but cannot be measured using HR-EBSD cross-correlation. The least square method minimized the extreme gradients and directed the stress distribution in each grain towards an equilibrium state with an assumption that the grains were stress free at the boundaries, i.e. no type-II stresses were present. From these two descriptions the direct method may be viewed as more physically correct because it goes some way to include the influence of the Type-II stresses but the ability of the least squares approach to reduce extreme stresses caused by error identified by the cross-correlation software proves useful in ensuring smooth gradients.

As noted in Fig. 13, before loading a select few grains showed similarities to the experimental distributions. These similarities may have arisen because the unknown type-II stresses in the regions surrounding the grains in question may have been similar so the assumption of zero type-II stress was more applicable in these specific areas. This hypothesis could be tested in future work if a Type-II stress measurement technique was used in conjunction with HR-EBSD cross-correlation.

The difference between modelling and experimental results may call into question the validity of the crystal plasticity model but the formulation and constitutive laws used here are well known and have been validated numerous times [15,39,40] hence why they were used in this work. The grain size effect was deemed necessary because Agius et al. [24] showed that including a grain size effect helped match experimental stress distributions near grain boundaries and replicating these local stress distributions is important for comparing intra-granular distributions.

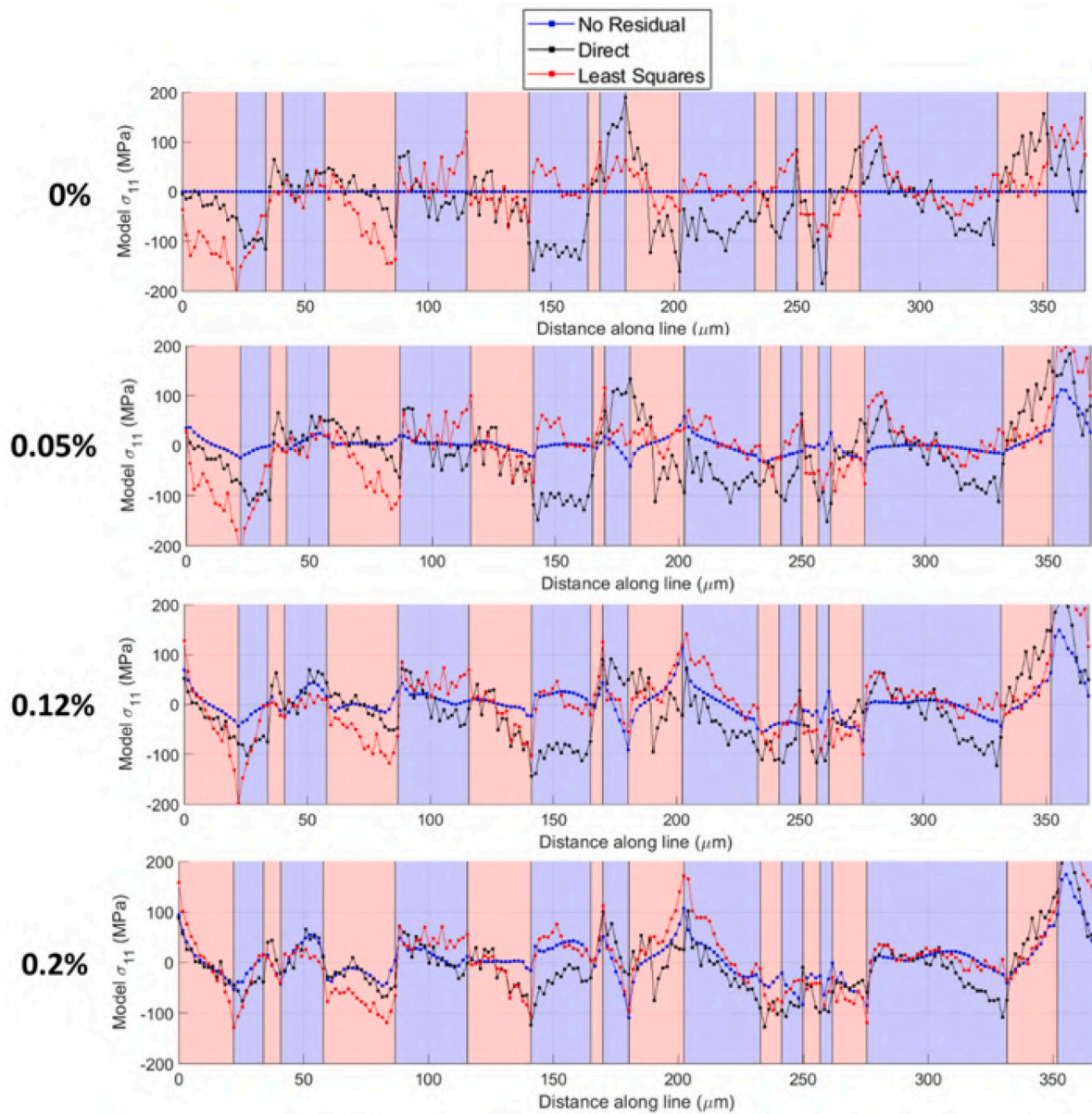


Fig. 17. Type-III stress line profiles taken along line 2 in Fig. 16a at different loading strains.

Another important behaviour that this work did not address is the evolution of the stress field during unloading. The experimental data collected is ex-situ only, and as such does not provide the information required to analyse this particular behaviour. There are facilities available that allow for in-situ testing using techniques similar to those described in this paper so future experiments could tackle this important question.

7. Conclusions

Using the method described by Kapoor et al. [7] pre-test residual stresses have been successfully included in the crystal plasticity formulation described. From the analysis undertaken, the following conclusions can be drawn:

- The direct method removed extreme stresses at boundaries but did not smooth the stress profiles in the grain interiors. In contrast, the least squares method used to satisfy equilibrium removed unreasonably extreme values of stress at grain boundaries

due to the traction free constraint whilst also helping the internal stress distributions reach equilibrium.

- After loading and unloading, the simulation with no initial residual stresses showed similar final distributions to both simulations that included residual stresses via a direct and least squares method. This indicates that the inclusion of Type-III initial stress profiles measured using HR-EBSD has minimal effect after loading. The stress magnitudes simulated did not match with the experimentally measured profiles in most locations.

This study has highlighted some potential drawbacks for incorporating residual stresses at the micro scale:

- The stresses that can be measured by HR-EBSD are type-III residual elastic; these measurements alone, as no knowledge of the type-II stresses is possible with this method, is insufficient to describe the initial intragranular stress state prior to simulation. The least squares approach was used as an attempt to alleviate this problem by ensuring each grain was in equilibrium before being applied to the model. This did remove extreme stress magnitudes

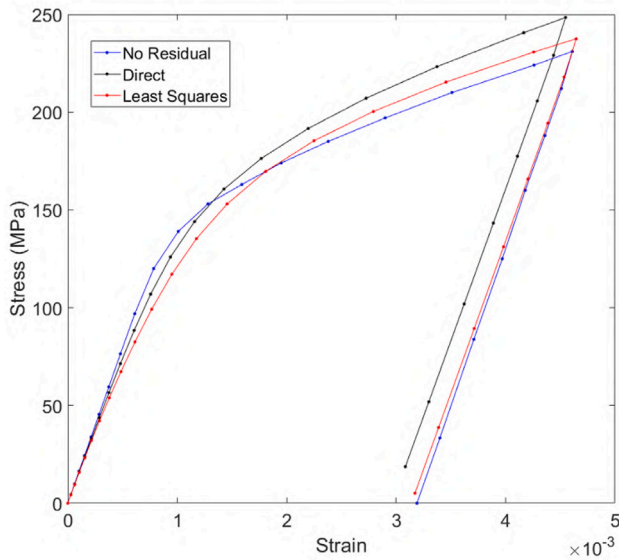


Fig. 18. Loading Curves produced from the three simulations assuming no prior knowledge of the stress distributions.

present but did not significantly improve the match between experimental and model results compared to the direct approach.

- The subsurface microstructure was unknown; using only a surface measurement proved insufficient to accurately predict the intragranular deformation of the material. As an attempt to mitigate this problem an oligocrystal structure was assumed, however, this has limited effectiveness as the influence of subsurface microstructure is not accounted for.

In future work using a technique that is able to measure both Type-II and III stresses, such as scanning XRD, may significantly improve the predictive capabilities of the crystal plasticity model described. Other options for collecting just type-II stress exist such as synchrotron XRD which could be used in conjunction with HR-EBSO cross-correlation to further improve surface measurements.

The 3D geometry must also be taken into consideration, either through manipulating the microstructure of samples, using 3D microstructural characterization techniques such as 3D EBSD or near-field 3DXRD or using robust statistical information to produce representative volume elements.

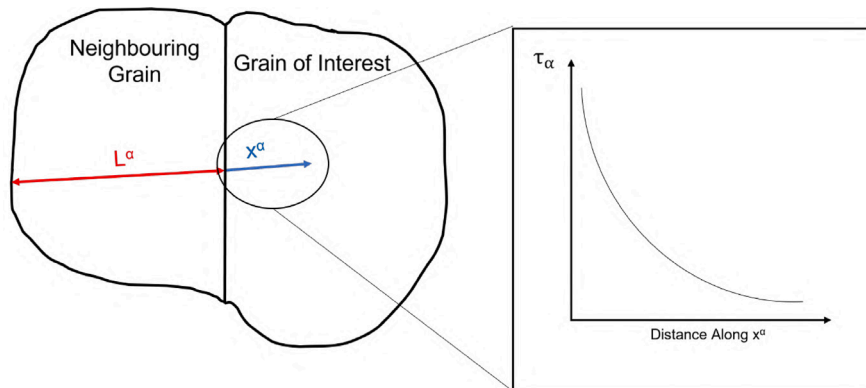


Fig. A.19. Depiction of how the grain size effect influences the stress pile-up τ_α as a function of distance. The size of grain the neighbouring grain (L^α) and the ease of slip between the two grains (k^α) influences the stress pile-up at the grain boundary.

CRediT authorship contribution statement

Edward William Horton: Conceptualization, Methodology, Software, Validation, Formal analysis, Writing – original draft, Visualization. **Eralp Demir:** Conceptualization, Methodology, Software, Writing – review & editing. **Dylan Agius:** Software, Writing – review & editing. **Anna Kareer:** Investigation, Software, Writing – review & editing. **David M. Collins:** Investigation, Software, Writing – review & editing. **Mahmoud Mostafavi:** Conceptualization, Writing – review & editing, Funding acquisition, Supervision. **David Knowles:** Conceptualization, Writing – review & editing, Funding acquisition, Supervision.

Declaration of competing interest

The authors declare that they have no known competing financial interests or personal relationships that could have appeared to influence the work reported in this paper.

Data availability

Data will be made available on request.

Acknowledgements

The Authors would like to thank EDF Energy and the Engineering Physical Sciences Research Council (EPSRC) for the support. The authors acknowledge the Advanced Computing Research Centre, University of Bristol (<https://www.bristol.ac.uk/acrc/>), which was used for the simulations presented in this study. Additionally, the authors would like to thank the efforts of Dr Chris Wallbrink from the Defence, Science and Technology Group (DSTG) for reviewing the manuscript.

Appendix. Grain size effect description

This formulation adds the influence of grain size by calculating the slip resistance, τ_c^α , at each point within a grain based on a lengthscale parameter, L^α , that corresponds to the length of the slip system α if that slip system was continuous into the neighbouring grain, as displayed in Fig. A.19. Eq. (A.1) sets out how the slip resistance is calculated.

$$\tau_c^\alpha = \tau_0^\alpha + \frac{k^\alpha}{\sqrt{L^\alpha}} \quad (\text{A.1})$$

k^α is the micro Hall–Petch coefficient that represents the ease of which slip can occur between the grain in question and its neighbour, using the formulation developed by Andani et al. [32],

$$k^\alpha = K(1 - m^{\alpha'})^c \quad (\text{A.2})$$

where K and c are fitting parameters. $m^{\alpha'}$ is the Luster-Morris parameter [41], which is introduced into the formulation to consider the inter-grain interaction of slip systems. This takes the slip plane normal \mathbf{n}_x^α and the slip direction \mathbf{s}_x^α for the grain of interest and the relevant neighbouring grain, (A.3).

$$m^{\alpha'} = \left(\frac{\mathbf{n}_A^\alpha \cdot \mathbf{n}_B^\alpha}{|\mathbf{n}_A^\alpha| |\mathbf{n}_B^\alpha|} \right) \left(\frac{\mathbf{s}_A^\alpha \cdot \mathbf{s}_B^\alpha}{|\mathbf{s}_A^\alpha| |\mathbf{s}_B^\alpha|} \right) \quad (\text{A.3})$$

To account for the distance from the grain boundary when calculating the stress pile-up (ahead of the boundary) Andani et al. [32] suggested the following relationship, representing the abrupt stress drop seen experimentally, Eq. (A.4).

$$\tau^\alpha = \left(\tau_0^\alpha + \frac{k^\alpha}{\sqrt{L^\alpha}} \right) \left[\frac{x^\alpha + \frac{L^\alpha}{2}}{\sqrt{\left(x^\alpha + \frac{L^\alpha}{2}\right)^2 - \left(\frac{L^\alpha}{2}\right)^2}} - 1 \right] \quad (\text{A.4})$$

where x^α is the distance from the grain boundary.

References

- [1] T.J. Turner, P.A. Shade, J.V. Bernier, S.F. Li, J.C. Schuren, P. Kenesei, R.M. Suter, J. Almer, Crystal plasticity model validation using combined high-energy diffraction microscopy data for a Ti-7Al specimen, *Metall. Mater. Trans. A* 48 (2) (2017) 627–647, <http://dx.doi.org/10.1007/s11661-016-3868-x>.
- [2] E. Salvati, T. Sui, A.M. Korsunsky, Uncertainty quantification of residual stress evaluation by the FIB-DIC ring-core method due to elastic anisotropy effects, *Int. J. Solids Struct.* 87 (2016) 61–69, <http://dx.doi.org/10.1016/j.jislostr.2016.02.031>, URL <https://www.sciencedirect.com/science/article/pii/S0020768316000937>.
- [3] E. Salvati, A. Korsunsky, An analysis of macro- and micro-scale residual stresses of type I, II and III using FIB-DIC micro-ring-core milling and crystal plasticity FE modelling, *Int. J. Plast.* 98 (2017) 123–138, <http://dx.doi.org/10.1016/j.jiplas.2017.07.004>, URL <https://www.sciencedirect.com/science/article/pii/S0749641917301377>.
- [4] E. Macherauch, Introduction to residual stress, in: A. NIKU-LARI (Ed.), *Residual Stresses*, Pergamon, 1987, pp. 1–36, <http://dx.doi.org/10.1016/B978-0-08-034062-3.50011-2>, URL <https://www.sciencedirect.com/science/article/pii/B9780080340623500112>.
- [5] S. Pratihari, M. Turski, L. Edwards, P. Bouchard, Neutron diffraction residual stress measurements in a 316L stainless steel bead-on-plate weld specimen, *Int. J. Press. Vessels Pip.* 86 (1) (2009) 13–19, <http://dx.doi.org/10.1016/j.jipvp.2008.11.010>, URL <https://www.sciencedirect.com/science/article/pii/S0308016108001634>, The NeT Residual Stress Measurement and Modelling Round Robin on a Single Weld Bead-on-Plate Specimen.
- [6] E. Salvati, H. Zhang, K.S. Fong, X. Song, A.M. Korsunsky, Separating plasticity-induced closure and residual stress contributions to fatigue crack retardation following an overload, *J. Mech. Phys. Solids* 98 (2017) 222–235, <http://dx.doi.org/10.1016/j.jmps.2016.10.001>, URL <https://www.sciencedirect.com/science/article/pii/S0022509616305531>.
- [7] K. Kapoor, M.D. Sangid, Initializing type-2 residual stresses in crystal plasticity finite element simulations utilizing high-energy diffraction microscopy data, *Mater. Sci. Eng. A* 729 (2018) 53–63, <http://dx.doi.org/10.1016/j.msea.2018.05.031>.
- [8] K.P. McNelis, P.R. Dawson, M.P. Miller, A two-scale methodology for determining the residual stresses in polycrystalline solids using high energy X-ray diffraction data, *J. Mech. Phys. Solids* 61 (2) (2013) 428–449, <http://dx.doi.org/10.1016/j.jmps.2012.09.015>.
- [9] W.D. Musinski, D.L. McDowell, On the eigenstrain application of shot-peened residual stresses within a crystal plasticity framework: Application to Ni-base superalloy specimens, *Int. J. Mech. Sci.* 100 (2015) 195–208, <http://dx.doi.org/10.1016/j.jimecsci.2015.06.020>.
- [10] T. Britton, A. Wilkinson, High resolution electron backscatter diffraction measurements of elastic strain variations in the presence of larger lattice rotations, *Ultramicroscopy* 114 (2012) 82–95, <http://dx.doi.org/10.1016/j.ultramic.2012.01.004>.
- [11] A.J. Wilkinson, G. Meaden, D.J. Dingley, High resolution mapping of strains and rotations using electron backscatter diffraction, *Mater. Sci. Technol.* 22 (11) (2006) 1271–1278, <http://dx.doi.org/10.1179/174328406X130966>.
- [12] A.J. Wilkinson, G. Meaden, D.J. Dingley, High-resolution elastic strain measurement from electron backscatter diffraction patterns: New levels of sensitivity, *Ultramicroscopy* 106 (4) (2006) 307–313, <http://dx.doi.org/10.1016/j.ultramic.2005.10.001>.
- [13] B. Britton, I. Holton, G. Meaden, D. Dingley, High angular resolution electron backscatter diffraction: measurement of strain in functional and structural materials, *Microsc. Anal.* 27 (4) (2013) 8–13.
- [14] K. Kapoor, Y.S.J. Yoo, T.A. Book, J.P. Kacher, M.D. Sangid, Incorporating grain-level residual stresses and validating a crystal plasticity model of a two-phase Ti-6Al-4V alloy produced via additive manufacturing, *J. Mech. Phys. Solids* 121 (2018) 447–462, <http://dx.doi.org/10.1016/j.jmps.2018.07.025>.
- [15] S. Kalidindi, C. Bronkhorst, L. Anand, Crystallographic texture evolution in bulk deformation processing of FCC metals, *J. Mech. Phys. Solids* 40 (3) (1992) 537–569, [http://dx.doi.org/10.1016/0022-5096\(92\)80003-9](http://dx.doi.org/10.1016/0022-5096(92)80003-9).
- [16] A. Beaudoin, K. Mathur, P. Dawson, G. Johnson, Three-dimensional deformation process simulation with explicit use of polycrystal plasticity models, *Int. J. Plast.* 9 (7) (1993) 833–860, [http://dx.doi.org/10.1016/0749-6419\(93\)90054-T](http://dx.doi.org/10.1016/0749-6419(93)90054-T).
- [17] D.-F. Li, C.M. Davies, S.-Y. Zhang, C. Dickinson, N.P. O'Dowd, The effect of prior deformation on subsequent microplasticity and damage evolution in an austenitic stainless steel at elevated temperature, *Acta Mater.* 61 (10) (2013) 3575–3584, <http://dx.doi.org/10.1016/j.actamat.2013.02.038>.
- [18] D. Raabe, M. Sachtler, Z. Zhao, F. Roters, S. Zaefferer, Micromechanical and macromechanical effects in grain scale polycrystal plasticity experimentation and simulation, *Acta Mater.* 49 (17) (2001) 3433–3441, [http://dx.doi.org/10.1016/S1359-6454\(01\)00242-7](http://dx.doi.org/10.1016/S1359-6454(01)00242-7).
- [19] F. Roters, P. Eisenlohr, L. Hantcherli, D. Tjahjanto, T. Bieler, D. Raabe, Overview of constitutive laws, kinematics, homogenization and multiscale methods in crystal plasticity finite-element modeling: Theory, experiments, applications, *Acta Mater.* 58 (4) (2010) 1152–1211, <http://dx.doi.org/10.1016/j.actamat.2009.10.058>.
- [20] F. Dunne, D. Rugg, A. Walker, Lengthscale-dependent, elastically anisotropic, physically-based hcp crystal plasticity: Application to cold-dwell fatigue in Ti alloys, *Int. J. Plast.* 23 (6) (2007) 1061–1083, <http://dx.doi.org/10.1016/j.jiplas.2006.10.013>.
- [21] J. Carmai, F. Dunne, Simple model for consolidation of metal matrix coated SiC fibre composites, *Mater. Sci. Technol.* 19 (7) (2003) 919–924, <http://dx.doi.org/10.1179/026708303225002910>.
- [22] D. Buchanan, R. John, R. Brockman, A. Rosenberger, A coupled creep plasticity model for residual stress relaxation of a shot peened nickel-base superalloy, *JOM: J. Miner. Met. Mater. Soc.* 62 (2010) 75–79, <http://dx.doi.org/10.1007/s11837-010-0016-8>.
- [23] A.J. Wilkinson, T.B. Britton, Strains, planes, and EBSD in materials science, *Mater. Today* 15 (9) (2012) 366–376, [http://dx.doi.org/10.1016/S1369-7021\(12\)70163-3](http://dx.doi.org/10.1016/S1369-7021(12)70163-3).
- [24] D. Agius, A. Kareer, A.A. Mamun, C. Truman, D.M. Collins, M. Mostafavi, D. Knowles, A crystal plasticity model that accounts for grain size effects and slip system interactions on the deformation of austenitic stainless steels, *Int. J. Plast.* 152 (2022) 103249, <http://dx.doi.org/10.1016/j.jiplas.2022.103249>.
- [25] R.D. McGinty, D.L. McDowell, Multiscale polycrystal plasticity, *J. Eng. Mater. Technol. Trans. ASME* 121 (2) (1999) 203–209, <http://dx.doi.org/10.1115/1.2812367>, URL <https://doi.org/10.1115/1.2812367>, Cited by: 54.
- [26] A. Khan, P. Cheng, An anisotropic elastic-plastic constitutive model for single and polycrystalline metals. I-theoretical developments, *Int. J. Plast.* 12 (2) (1996) 147–162, [http://dx.doi.org/10.1016/S0749-6419\(96\)00001-0](http://dx.doi.org/10.1016/S0749-6419(96)00001-0), URL <https://www.sciencedirect.com/science/article/pii/S0749641996000010>.
- [27] M.F. Horstemeyer, D.L. McDowell, Modeling effects of dislocation substructure in polycrystal elastoviscoplasticity, *Mech. Mater.* 27 (3) (1998) 145–163, [http://dx.doi.org/10.1016/S0167-6636\(97\)00037-9](http://dx.doi.org/10.1016/S0167-6636(97)00037-9), URL <https://www.sciencedirect.com/science/article/pii/S0167663697000379>.
- [28] P.J. Armstrong, C. Frederick, et al., A Mathematical Representation of the Multiaxial Bauschinger Effect, Vol. 731, Central Electricity Generating Board [and] Berkeley Nuclear Laboratories ..., 1966.
- [29] R. Asaro, A. Needleman, Overview no. 42 texture development and strain hardening in rate dependent polycrystals, *Acta Metall.* 33 (6) (1985) 923–953, [http://dx.doi.org/10.1016/0001-6160\(85\)90188-9](http://dx.doi.org/10.1016/0001-6160(85)90188-9).
- [30] D. Peirce, R. Asaro, A. Needleman, Material rate dependence and localized deformation in crystalline solids, *Acta Metall.* 31 (12) (1983) 1951–1976, [http://dx.doi.org/10.1016/0001-6160\(83\)90014-7](http://dx.doi.org/10.1016/0001-6160(83)90014-7).
- [31] D. Agius, A.A. Mamun, C.A. Simpson, C. Truman, Y. Wang, M. Mostafavi, D. Knowles, Microstructure-informed, predictive crystal plasticity finite element model of fatigue-dwells, *Comput. Mater. Sci.* 183 (2020) 109823, <http://dx.doi.org/10.1016/j.commatsci.2020.109823>.
- [32] M.T. Andani, A. Lakshmanan, M. Karamooz-Ravari, V. Sundararaghavan, J. Allison, A. Misra, A quantitative study of stress fields ahead of a slip band blocked by a grain boundary in unalloyed magnesium, *Nature* 10 (1) (2020) 3084, <http://dx.doi.org/10.1038/s41598-020-59684-y>, URL <https://doi.org/10.1038/s41598-020-59684-y>.
- [33] P.J. Withers, H. Bhadeshia, Residual stress. Part 1—measurement techniques, *Mater. Sci. Technol.* 17 (4) (2001) 355–365.
- [34] K.P. McNelis, P.R. Dawson, M.P. Miller, A two-scale methodology for determining the residual stresses in polycrystalline solids using high energy X-ray diffraction data, *J. Mech. Phys. Solids* 61 (2) (2013) 428–449.
- [35] E. Demir, J.-S. Park, M. Miller, P. Dawson, A computational framework for evaluating residual stress distributions from diffraction-based lattice strain data, *Comput. Methods Appl. Mech. Engrg.* 265 (2013) 120–135.

- [36] E. Demir, H.S. Sas, M. Isik, E.A. Gungor, K. Davut, A numerical methodology for monitoring stress distributions and experimental proof of the concept on metal embedded thin polymer-matrix composites using X-ray diffraction, *Thin-Walled Struct.* 173 (2022) 108942.
- [37] M.A. Groeber, M.A. Jackson, DREAM.3D: A digital representation environment for the analysis of microstructure in 3D, *Integr. Mater. Manuf. Innov.* 3 (1) (2014) 56–72, <http://dx.doi.org/10.1186/2193-9772-3-5>, URL <https://doi.org/10.1186/2193-9772-3-5>.
- [38] Y. Hayashi, D. Setoyama, Y. Hirose, T. Yoshida, H. Kimura, Intragranular three-dimensional stress tensor fields in plastically deformed polycrystals, *Science* 366 (6472) (2019) 1492–1496, <http://dx.doi.org/10.1126/science.aax9167>, arXiv: <https://www.science.org/doi/pdf/10.1126/science.aax9167>, URL <https://www.science.org/doi/abs/10.1126/science.aax9167>.
- [39] L. Delannay, P.J. Jacques, S.R. Kalidindi, Finite element modeling of crystal plasticity with grains shaped as truncated octahedrons, *Int. J. Plast.* 22 (10) (2006) 1879–1898, <http://dx.doi.org/10.1016/j.ijplas.2006.01.008>, URL <https://www.sciencedirect.com/science/article/pii/S0749641906000118>, Cited by: 141.
- [40] A. Salem, S. Kalidindi, S. Semiatin, Strain hardening due to deformation twinning in α -titanium: Constitutive relations and crystal-plasticity modeling, *Acta Mater.* 53 (12) (2005) 3495–3502, <http://dx.doi.org/10.1016/j.actamat.2005.04.014>, URL <https://www.sciencedirect.com/science/article/pii/S1359645405002168>.
- [41] L. J., M. M.A., Compatibility of deformation in two-phase Ti-Al alloys: Dependence on microstructure and orientation relationships, *Metall. Mater. Trans. A* 26 (7) (1995) 1745–1756, <http://dx.doi.org/10.1007/BF02670762>, Cited by: 223.